Accepted manuscript of
The uncertainty of local flow parameters during inundation flow over complex topographies with elevation errors
by
Ryota Tsubaki and Yoshihisa Kawahara
published in
Journal of Hydrology
Volume 486, 12 April 2013, Pages 71–87
DOI: 10.1016/j.jhydrol.2013.01.042

The Uncertainty of Local Flow Parameters During Inundation Flow Over Complex Topographies with Elevation Errors

by

Ryota Tsubaki[*1] and Yoshihisa Kawahara[1]

*** Corresponding author, Phone/Fax 81-82-424-7847, Mail rtsubaki@hiroshima-u.ac.jp**

1 Department of Civil and Environmental Engineering, Hiroshima University,

1-4-1 Kagamiyama, Higashi-hiroshima, 739-8527, Japan

Abstract

Since the topographical data obtained from LiDAR (Light Detection and Ranging) measurements is superior in resolution and accuracy as compared to conventional geospatial data, over the last decade aerial LiDAR (Light Detection and Ranging) has been widely used for obtaining geospatial information. However, digital terrain models made from LiDAR data retain some degree of uncertainty as a result of the measurement principles and the operational limitations of LiDAR surveying. LiDAR cannot precisely measure topographical elements such as ground undulation covered by vegetation, curbstones, etc. Such instrumental and physical uncertainties may impact an estimated result in an inundation flow simulation. Meanwhile, how much and how these topographical uncertainties affect calculated results is not understood. To evaluate the effect of topographical uncertainty on the calculated inundation flow, three representative terrains were prepared that included errors in elevation. Here, the topographical uncertainty that was introduced was generated using a fractal algorithm in order to represent the spatial structure of the elevation uncertainty. Then, inundation flows over model terrains were calculated with an unstructured finite volume flow model that solved shallow water equations. The sensitivity of the elevation uncertainty on the calculated inundated propagation, especially the local flow velocity, was evaluated. The predictability of inundation flow over complex topography is discussed, as well as its relationship to topographical features.

Keywords: inundation simulation, complex topography, LiDAR, shallow water flow model, LIC, water level profile.

1. Introduction

Aerial LiDAR (Light Detection and Ranging) measurements have been widely used for obtaining topographical data. LiDAR measurements allow one to survey the distribution of ground surface elevation (e.g. Bates, 2003) and the bathymetry under water surfaces (McKean et al., 2009). Spatial resolution and elevation accuracy are greatly enhanced as compared to conventional surveying methods. As compared with aerial LiDAR, terrestrial LiDAR is also a powerful tool for obtaining complex geometry using a higher density and accuracy.

Numerical flow simulations have achieved great strides in solving flow equations stably and accurately (Alcrude and Garcia-Navarro, 1993; Anastasiou and Chan, 1997; Caleffi et al., 2003). The development of computational speed and the popularization of an efficient coding technique (e.g. OpenMP (Open MultiProcessing) or MPI (Message Passing Interface)) enabled us to conduct detailed and realistic inundation flow simulations using accurate flow models and high-resolution calculation grids that were based on detailed topographical data (Cobby et al., 2003; Soares-Frazão et al., 2008; Schubert et al., 2008; Neal et al., 2010; and Sanders et al., 2010).

LiDAR is a high-resolution and accurate method for obtaining topographical data (Néelz et al., 2006; Mason et al., 2007), even though the spatial resolution and the elevation accuracy have restrictions as a result of operational and device limitations. Typically, since aerial LiDAR detects the ground surface from the sky, elevations of ground surfaces under vegetation cover or buildings cannot be measured directly (Figure 1). Also difficult is precisely measuring small-scale topographical elements such as planted vegetation on roadsides, and the distribution of parked cars and curbstones that have some impact on inundation flows (Bales and Wagner, 2009, Mignot et al., 2006). The LiDAR survey provides massive numbers of data points (point cloud; Sithole and Vosselman 2004), then the digital terrain models is generated by the spatial reconstruction of LiDAR point data. In the area close to buildings or under the elevated road, laser from sky is unable to reach to the ground surface. In the ground surface covered by vegetation, some laser pulse is able to arrive to the ground but the point density of true ground returns is drastically reduced due to leaf interference. Due to these limitations, digital terrain models made from LiDAR data result in non-negligible uncertainty, and, in turn, impact the predicted behavior of inundation flow (e.g. impact of elevated road is discussed in Abdullah et al. 2011). The effects of uncertainties for inflow and roughness parameters were explored in Schumann et al. (2008), Pappenberger et al. (2009), and Bales and Wagner (2009). The uncertainties for inflow have been estimated and the range has been gradually reduced based on advancements in hydrological modeling (e.g. Shamseldin, 1997; Chuntian et al., 2002; Wagener et al., 2003; Wu et al., 2009). The effect and the parameterization of the roughness coefficient within the flood plain were a classical key point in the inundation flow simulation; and within a number of references discussed on this point (e.g. Neal et al., 2009; Casas et al., 2010; and Stephens et al., 2012). On the other hand, the effect of elevation uncertainty on the predicted flow is not yet quantitatively understood (Sanders, 2007).

Another point not sufficiently understood is the uncertainty of predicted velocity. Many have discussed uncertainty in the predicted inundated area, the water stage, the friction factor, and those relationships (e.g, Pappenberger et al., 2005; Horritt, 2006; and Schumann et al., 2007). The inundated area and the inundated water stage are significant indicators for risk estimations; however, uncertainty in velocity has not been addressed well as a result of a lack of an accurate field record indicating flow velocity during inundation. Propagation of the inundated area has been observed as a result of flow motion. Therefore, essentially, the validation of flow motion must be implemented. Unfortunately, it is likely that the inundated area is accurately predicted without an accurate prediction of the dynamic process (flow motion) because the maximum inundated area is almost determined as hydrostatic.

In this work, inundation flow on three representative terrain models, with and without artificial elevation error, was evaluated in order to systematically and quantitatively evaluate the effect of elevation uncertainty on the calculated inundation flow. A high-resolution grid (3 m in spacing) calculation was treated as a benchmark following a sensitivity analysis on grid spacing. The accuracy of the predicted result was evaluated based not only on the inundated area and the water depth, but also on the velocity and flow momentum. The predictability of inundation flow over actual topography is also discussed.

2. Numerical flow model

In this work, two-dimensional (2D) shallow-water equations were solved using a shock-capturing, finite-volume scheme on an unstructured triangulate grid system (Tsubaki et al., 2008; Tsubaki and Fujita, 2010). The following fundamental equations were used:

$$\frac{\partial h}{\partial t}+\frac{\partial hu}{\partial x}+\frac{\partial hv}{\partial y}=0, \tag{1}$$

$$\frac{\partial uh}{\partial t}+\frac{\partial u^2 h}{\partial x}+\frac{\partial uvh}{\partial y}+\frac{g}{2}\frac{\partial h^2}{\partial x}-gh\frac{\tau_{sx}-\tau_{bx}}{\rho}=0, \tag{2}$$

$$\frac{\partial vh}{\partial t}+\frac{\partial uvh}{\partial x}+\frac{\partial v^2 h}{\partial y}+\frac{g}{2}\frac{\partial h^2}{\partial y}-gh\frac{\tau_{sy}-\tau_{by}}{\rho}=0 \tag{3}$$

where h is the depth of flow, u and v are the depth-averaged velocity components in the x and y directions, t is the time, and g is the gravitational acceleration. τ_{bx} and τ_{by} are related to the bed slopes in the x and y directions, and τ_{sx} and τ_{sy} are the bottom shear stresses, which are defined as follows:

$$\frac{\tau_{bx}}{\rho}=-\frac{\partial z_b}{\partial x},\ \frac{\tau_{by}}{\rho}=-\frac{\partial z_b}{\partial y},\ \frac{\tau_{sx}}{\rho}=\frac{n^2 u\sqrt{u^2+v^2}}{h^{4/3}},\ \frac{\tau_{sy}}{\rho}=\frac{n^2 v\sqrt{u^2+v^2}}{h^{4/3}} \tag{4}$$

where n is Manning's roughness coefficient and z_b is the local ground elevation.

The finite volume method was used to discretize the fundamental equations in the same manner as utilized in Shige-eda et al. (2002) and Shige-eda and Akiyama (2003). The unknown variables were defined at the center of each cell. In order to ensure numerical stability, a flux difference scheme was adopted for the advection and source terms in the basic equations. The permeability of the building was neglected and the slip-wall condition was specified along the boundaries of the buildings. The treatment corresponds to the building-hole (BH) method as defined in Schubert and Sanders (2012). The topography of the domain was accounted for in the calculation as (1) the shape of the wall boundary, (2) the distribution of the cell averaged ground elevation z_b, and (3) the cell representative roughness parameter n. The work presented here focused on the effect of the topographical representation uncertainty, in particular, the error in the distribution of the ground elevation, z_b.

3. Topographical data processing

3.1 The artificial elevation error model

Topographical uncertainties are caused by various factors including systematic and random errors. In this study, based on the fact that the uncertainty of local ground elevation is highly affected by the topography and ground cover (Sithole and Vosselman 2004) as shown in Figure 1, an artificial elevation error, not just random but having spatial structure, was generated using a fractal algorithm (e.g. Bates et al., 1998). The fractal algorithm adopts the midpoint displacement algorithm using a diamond-square algorithm (see Figure 2, Fournier et al., 1982). The basic concept of the algorithm consists of the following: (1) interpolation of the central points in the square grid (Figure 2a and b), and (2) the interpolation of the central points in the diamond grid (Figure 2b and c). A pair of the square grid and the diamond grid interpolations composes one iteration step. The grid point number increases according to interpolation implementations. The interpolation was conducted n_i times to obtain the required grid point number of the topography. At the first few iteration steps, n_f, the interpolation of the elevation was operated as the mean value of four surrounding points. Following iteration steps over n_f steps, additional elevation error was introduced in the interpolated value. The magnitude of the elevation error is adjusted depending on the iteration step, namely the error magnitude B_i is calculated based on the magnitude of the previous step as $B_i = b\,B_{i-1,}$ where B_i is the error magnitude at iteration step i, and b (<1) is the reduction rate of the error magnitude per iteration step. The initial grid is a square grid that consists of 2×2 points and the elevation of the four initial points are set as 0 m. In the first n_f steps, the elevation noise is not introduced, so the topography in the first phase is just flat but the grid points are increased exponentially. After n_f steps, elevation error is introduced so that the topography begins to have undulation. The error magnitude is gradually decreased so that larger scaled undulation has a larger magnitude in the elevation, and the smaller scaled undulation has a smaller magnitude in elevation. In this work, the parameters were set as n_i = 9, n_f = 5, and b = 0.80 by considering the balance between the randomness and the

regularity of the model error. Here, a generated fractal pattern has grid points of $2^9 \times 2^9$. A factor of 1.953 m was set as the grid spacing for the *x* and *y* directions, and a domain of 1000 m × 1000 m for the noise pattern was generated as shown in Figure 3. The generated terrain model shows a structure whose spatial scale ranges from 1.953 m to $1.953\text{m} \times 2^4 = 31.248$ m. Elevation uncertainty in aerial LiDAR measurements depends on device performance and measurement conditions. Bales and Wagner (2009) reported that the uncertainty was less than 30 cm, while Néelz et al. (2006) estimated that the uncertainty in the root mean square was less than 15 cm. Therefore, the typical magnitude of LiDAR elevation error could be 0.15 m; so, in this work, 2σ was specified as 0.15 m. The error distribution $e(x, y)$ is generated based on the random numbers so standard deviation σ_e of distribution $e(x, y)$ can not to be determined in advance to generate error distribution. To adjust the error magnitude as $2\sigma_{e'} = 0.15$ m for the final error pattern $e'(x, y)$, correction

$$e'(x, y) = 0.15 e(x, y) / 2\sigma_e \quad (5)$$

was operated. Manning's roughness coefficient *n* was set to 0.01 in all cases. A larger Manning *n* is necessary in large grid size calculations and the sensitivity of the roughness coefficient to the calculated results is reduced in high-resolution calculations. The latter comes from the fact that detailed topographical features and small-scale flow structures are directly resolved in the flow simulation within fine grid systems (Casas et al. 2010). The roughness coefficient was treated to a constant and elevation uncertainty. The uncertainty of the roughness parameter and its effects on the calculated results are not discussed in this work.

3.2 The three terrain models

Three terrain models were used to explore the relationship among topographical types, inundation flow characteristics, and inundation prediction uncertainty. The first terrain model contained a series of flat terrains with a specific general ground slope. The model elevation uncertainty was overlain onto the base topography (see Figure 4). In this work, this topography set is called Plain topography. The second model set, shown in Figure 5, contained a series of topographies representing rice fields, a typical rural topography in Japan. This topography type was based on the DEM (digital elevation model) with a spatial resolution of 2 m, measured by an aerial LiDAR survey. In this work, this topography is called Rural topography. Each rice paddy parcel was separated by ribbing, forming a rectangular grid in the horizontal plane. As shown in Figure 6, the third model contained an urban topography that included a complex street network and buildings, and is referred to as Urban topography. The ground elevation of Urban topography was set as flat, with a specific ground slope as for Plain topography. The topology of the street and building arrangement was based on 1 m resolution LiDAR data. The vector data of each building shape was extracted from the DSM (digital surface model) and the DEM (Tsubaki and Fujita, 2010). The extracted vector data set was used as

184 the shape of the slip wall boundary in the unstructured grid. However, the detail of the elevation
185 distribution in actual urban areas is omitted in this work so that we could concentrate on the effect of
186 elevation uncertainty on the calculated results. The effects of this simplification were evaluated, in
187 detail, by Mignot et al., 2006. As measured by aerial LiDAR measurements, topography patterns
188 used in the second and third models were based on actual topography. Additional ground slope and
189 elevation uncertainties were overlain onto the elevation distribution. Flows calculated with a series
190 of topographies were compared with one another in order to evaluate the sensitivity of the general
191 ground slope and the elevation uncertainty on the predicted flow. The three topography sets were
192 discretized in the triangulate grid, where each grid size was 3, 5, 10, and 20 m. Variation in the grid
193 size was utilized to evaluate the sensitivity of the grid size on the calculated flow. The fundamental
194 effects of grid size on calculated results have been reported previously by, for example, Horritt and
195 Bates, 2001; Horritt et al., 2006; and Tsubaki et al., 2007. For specifying the grid size discussed in
196 the following text, the values “03 m”, “05 m”, “10 m”, and “20 m” are used in the figures and the
197 text. The three error patterns are specified as “ErrorA”, “ErrorB”, and “ErrorC”. The algorithm used
198 to generate three error patterns was identical and overall the error magnitude, $\sigma_{e'}$, was also identical
199 but a different table of random numbers was employed. Therefore, the spatial distribution of the
200 pattern differed completely for evaluating the universal effect of elevation error, not only error
201 pattern dependent features. Obviously, the actual spatial pattern of the topographical error is
202 impossible to identify in practice. Thus, unique effects due to specific error patterns are separated in
203 this work using three different error patterns, and the typical universal effects caused by elevation
204 error are discussed.
205 For the inflow boundary of each topography case, a steady flow rate, Q, of 50 m^3/s (Plain), 30 m^3/s
206 (Rural), and 25 m^3/s (Urban) was configured. The lengths of the inflow boundaries were 20 m
207 (Plain), 20 m (Rural), and 25 m (Urban). Inflow conditions modeled sudden inundation due to rapid
208 embankment breaching.
209
210 **4. Result**
211 In this section, the grid size effect in the expansion of an inundated area was investigated in order to
212 validate the flow model. Then, the effects of elevation error and grid size on the Plain, Rural, and
213 Urban topographies are discussed. Finally, the effects of topographical uncertainty on calculated
214 local flow parameters are explored.
215
216 **4.1 Grid size effects**
217 In this subsection, the grid size effect on the propagation of inundation water is explored for
218 validating the flow model that included both the discretized fundamental equations and the
219 calculation grid (Bales and Wagner 2009). The topographical data discussed in this subsection

retained no elevation error.

4.1.1 Plain topography

In Figure 7, hydrographs of water volume in the calculation domain, using different grid sizes, are depicted. As shown in the figure, the inundation water volume was not sensitive to grid size and was consistent with the exact value (i.e. $V = Qt$, where V is the water volume (m^3), Q (= 20 m^3/s) is the inflow discharge, and t is the elapsed time (s) after inundation begins. The results indicate that the numerical model, including the treatment of the wet-dry boundary, was perfectly conservative, at least in mass.

Time-series changes of the inundated area in the various grid sizes and for the two bed slopes are compared in Figure 8. As shown in Figure 8a, for the case of a medium slope, a low sensitivity for the grid size to the expansion of an inundated area was observed (a 5% difference between the 03 m and 20 m grids). The results of the 03 m and 05 m grids were approximately identical (a 0.5% difference in the inundated area). The results of the milder slope cases (I = 1/1000 and I = 1/2000) are not provided here, however, the profile was quite similar to Figure 8a. In the case of a steep slope (I = 1/50, as shown in Figure 8b), the hydrograph of the inundated area differed along with the grid size. The graph indicates that the result, calculated using a smaller grid size, displayed a smaller inundation area. In order to investigate the cause of inadequate behaviour, as observed for the steep slope case, snap-shots of inundated water depth for the small and large grid cases at the same instant (t = 200 s) are presented in Figure 9. The result of the small grid (in the upper half of Figure 9) is longer and thinner in the downslope direction in the shape of the inundated area, as compared to those of the coarse grid result depicted in the lower half of Figure 9. For the steep slope condition, flow was determined at the upstream side because the flow was super-critical, and the propagation pattern of inundation flow is sensitive to the local flow surrounding the inflow boundary. As indicated in Figure 9, the angle of expansion of the flow surrounding the inflow point in the coarse grid result was larger than that of the fine grid case. In cases of milder slope, the propagation pattern is mainly governed by a water surface slope surrounding the propagating edge and is insensitive to local flow at the inflow point. The difference in the mechanism of expansion of inundation water, depending on the general ground slope, caused a difference in the sensitivity of the grid size to the propagation of inundation.

In conclusion, in this subsection, a grid size smaller than 10 m was sufficient for representing the rapid expansion of inundation water for Plain topography with a 20 m width inflow boundary. On the other hand, a grid size finer than 10 m was needed in order to resolve the sudden change of flow, in case local transient flow has a major impact on the expansion of the inundated area.

4.1.2 Rural topography

In Figure 10, two time-series for the inundated area, calculated using fine (03 m) and medium (05 m) grids, are compared. The general trends for the inundated area expansion are identical to one another, but the result calculated using the 05 m grid was overestimated by a few percent, as compared with the result of 03 m. The overestimation trend in the larger grid result was similar to the result observed for Plain topography with a steep slope (see Figure 8b). In Figure 11, the instantaneous distributions of water depth, as calculated using the 03 m and 05 m grids at t = 1000 s, are depicted. The general pattern for water depth was quite analogous but a difference was observed surrounding the wet-dry boundary. In this area, due to a small water depth, the flow was quite sensitive to the small difference in ground elevation and led to the difference in the time series change in the inundated area. In Figure 12, histograms of water depth at t = 1000 s for the 03 m and 05 m cases are provided. Differences were observed in the shallow region (h < 0.1m). However, the profiles, with the exception of the shallow region, were almost similar.

In summary, for Rural topography, a difference between the 03 m and 05 m results was observed in the area surrounding the outline of the inundated area. However, the general propagation pattern of inundation was insensitive to grid size in the range below 5 m. Rural topography was represented by the distinguishing ground undulation pattern, which has a spatial scale over a few meters and regulates the inundation expansion pattern. Thus, the pattern of the calculated inundation expansion was almost insensitive to the grid size if the discretised grid represented the distinguishing ground pattern.

4.1.3 Urban topography

Urban topography was represented by building arrangement and sloped ground. In Figure 13, the time-series of the inundated area for the steep sloped case (I = 1/50) and the mild sloped case (I = 1/1000) are depicted. For both steep and mild slope cases, the time-series change of the inundated area was insensitive to grid size. In Figure 14, the distributions of water depth at t = 400 s, as calculated by the 03 m and 05 m grids, are compared. The distributions of the two grid sizes are generally identical. The result supports the idea that the calculated results of urban topography are insensitive to grid size because the unstructured grid is capable of representing the irregular shape of a complex building boundary and because the representation of the building boundary is less subject to the difference in grid size, since an unstructured grid system is used.

4.2 The impact of elevation error in Plain topography

In Figure 15, water depth distributions of inundation flows on different ground slopes, with and without artificial elevation errors, are depicted. Even if the error is added, the topography in this

292 section is almost flat. Therefore, the inundated area expands rapidly with shallow water depth. In
293 cases where steep slopes exist (the upper contours of Figure 15), the inundated water flows in the
294 down-slope direction (the right side) rapidly, and the inundated area reaches 2,000 m from the
295 inflow point in the down-slope direction at t = 300 s.
296 In cases of a mild slope condition (the bottom contours in Figure 15), the inundated areas expand
297 concentrically near the inflow area and the inundated water depth is, in general, quite shallow (h <
298 0.1 m for most areas). The magnitude of the elevation error in the ErrorA case is 0.15 m, so the
299 magnitude of the water depth is equal in magnitude to the elevation error (Pasternack et al., 2006),
300 and the water flowing on the Plain topography with the elevation error suffers a major impact due to
301 elevation error. For the steep slope case, the relative impact due to elevation error impact is limited
302 as compared with those of milder slope cases.
303 Figure 16 compares the time-series changes of the inundated area calculated using a 03 m grid but a
304 different bed slope and error patterns. The results of the steep slope (I = 1/50) with and without
305 model error were almost identical. The results of the milder slope cases (I = 1/300 and I = 1/1000)
306 indicated a larger impact on inundation propagation due to elevation error. The effect of error
307 addition emerged as an underestimation of the inundated area. A small undulation disturbed the
308 inundation flow propagation. In addition, dents formed by elevation error impounded the water
309 volume, which spread faster in cases of an original flat topography. In Figure 17, the distributions of
310 the Froude number in cases of I = 1/300 and I = 1/1000, at t = 300 s, are compared. The inundation
311 flow in a case of I = 1/300 without error (the upper-left figure in Figure 17) was super-critical in
312 almost all areas. The area close to the inflow point was also super-critical for the I = 1/1000 case (the
313 lower-left figure in Figure 17), but the expanding front was sub-critical in this case. The results
314 calculated using elevation error showed a completely different distribution. The Froude number is
315 one of the key factors in water propagation for the shallow water condition. In the case of inundated
316 water spreading broadly in the horizontal and thinly in depth, the flow is quite sensitive to the small
317 undulation of ground elevation. As shown in Figure 17, inundation flow structure is drastically
318 changed due to elevation error. The topography data obtained using LiDAR contains elevation error,
319 and this error causes (i) an underestimation of the expansion of the inundated area, and (ii) a change
320 in the flow direction of inundation. The undulation, whose spatial scale is smaller than the grid size,
321 is filtered out during grid generation; however, the undulation, whose spatial scale is larger than the
322 grid size, is represented by the calculation grid. Undulation is due both to the originated topography
323 and the measurement error. The effect of small scale topographical features on the flow is modelled
324 in the roughness parameter within the numerical model. Small scale undulation, due to the error,
325 causes a limited effect on the flow because small undulation is filtered out during the gridding
326 process. Large scale elevation uncertainty, caused by structural or systematic error (e.g. the effect of
327 vegetation cover) leads to a considerable difference in the propagation pattern of inundation.

4.3 The effect of grid size and elevation uncertainty on Rural topography

In Figure 18, inundated flow structures calculated using different grid size and error patterns are compared. The structure of the flow is depicted using the Line Integral Convolution (LIC) method (Cabral and Leedom, 1993). LIC is a texture based flow visualization method. The direction of the texture in Figure 18 corresponds to the local flow direction. The contrast of the texture correlates with the flow rate per unit width, hU. The results obtained from the four cases, in general, show a similar structure. Inundated water overflows on the ribbing, and a critical flow and the control section are formed above the ribbing. The similar flow structure is represented regardless of the noise addition. However, as shown in Figure 18, the location where inundated water overflows to a neighboring paddy parcel differs depending upon the difference of grids.

The pattern of the flow route and the circulation observed within each rice field cell is quite complex and differs when the grid size and the elevation error pattern are changed, indicating that the flow structure within the rice field cell is quite sensitive to topographical uncertainty and is difficult to correctly predict. Although flow structure within the rice field cell affects damage to the planted crop, the global inundation propagation is less subjected to flow circulation within the rice-paddy cell, so the general pattern of expansion of the inundation is identical regardless of grid size and error pattern changes, as confirmed in Figure 18.

Figure 19 compares the time series change of the inundation area calculated using a 03 m grid and different elevation error patterns. The figure shows that the addition of elevation error causes a slight underestimation in the expansion of the inundation area. A minor difference was observed in the distribution of the inundated area (as shown in Figure 18). The underestimation trend in the inundated area following error appending was also observed for Plain topography (Figure 16). An underestimation in Rural topography was caused by flow disturbance and water storage effects (the effect of the latter was discussed in Horritt and Bates, 2001).

In conclusion, the general structure of inundation flow regulated by the structure of topography in a rural area, as shown in Figure 18, consisting of rice paddy cells and ribbings, is represented using detailed topographical data. However, the circulation of flow within each rice paddy, as well as the exact location of overflows that arise on ribbings, are quite sensitive to small differences in the topographical representation. In this sense, local flow parameters, especially the local velocity and the momentum of inundation flow within complex topographies are quite difficult to estimate. As a result, one must pay attention to difficulties in the prediction of local flow when implementing risk estimations based on local flow parameters, e.g. the assessment of risk that is related to the flow intensity (e.g. Koshimura et al. 2009), the estimation of sediment transport in the flood plain, etc.

4.4 The effect of grid size and elevation uncertainty on Urban topography

Urban topography consists of a complex impermeable boundary wall that represents buildings concentrated in a dense state. The ground is flat but has a constant bed slope (see Table 1). As described in Section 3.1, cases with error contain a small undulation in the elevation distribution. Figure 21 shows the time series of the inundated area calculated using grids with and without elevation error. The steep sloped result (Figure 21a) shows the very slight effect of elevation error on inundated area expansion. The medium slope result (Figure 21b) shows a greater influence for elevation error in the expansion of the inundation area as compared to the results from steep slope cases. The elevation error causes an approximate 25% underestimation in the growth of the inundation area in the medium slope case. The trend has already been observed for Plain topography (as discussed in Figure 16), and Rural topography (depicted in Figure 19). Results for the I = 1/1000 case of Urban topography are not depicted in Figure 21. However, the trend is similar to the result of the I = 1/300 case. Namely, a certain level of under-estimation (35%) of inundation area expansion was observed for a condition of I = 1/300 with elevation errors. As discussed in Section 4.2, the underestimation is due to the impact of both flow disturbance and water storage by the undulation formed due to elevation error.

In Figure 22, the flow structures of the urban floodplain, calculated using six different calculation grids, are depicted using the LIC method. The major water volume of inundated flow propagates throughout a broad street (depicted as a high contrast hair-line pattern in the street shown in Figure 22). Not only the broad street, but small streets connected to the broad street also contributed to spreading the inundated water, and a complex flow network bounded by urban topography emerged. As depicted in Figure 22, the structure of the flow is basically identical for the six cases. Differences in the ground slope impacted the degree of lateral dispersion of inundation flow, but the sensitivity of the ground slope changed and the difference in the propagation pattern was limited as compared with the result for Plain topography (see Figure 15). The inundation flow expansion was affected by grid size and elevation error in a similar manner as observed for the Plain and Rural cases, but sensitivity to grid size and elevation error was limited as compared to the Urban case.
In Figure 23, close-up images of the flow structure surrounding the inflow area are compared. Observed again is that the general flow structure is not sensitive to grid size and elevation error. However, the detail for the flow network in the small street system was impacted by differences of grid size and elevation.

4.5 *The flow prediction uncertainty*

In this section, the uncertainty of flow information, estimated using the flow simulation by considering the topographical uncertainty, is quantitatively discussed. In order to compare

instantaneous and local flow conditions between calculated results with different grid sizes, the flow parameters were interpolated on the grid at a 20 m interval in the x and y directions. In order to obtain the flow data at each grid point, cells whose centers were located within 5 m of the grid point were selected. Then, the mean of the flow parameters of the selected cell center values were calculated. For cases in which all cells close to the grid point were dry or quite shallow in water depth (h < 0.05m), the flow information at this grid point was not used in the following statistical calculation. The differences of the flow parameters (water depth, h; water level, H; flow rate per unit width, hU; and the momentum flux per unit width, hUU) between the two calculation cases for the entire corresponding grid points were calculated; then, the standard deviation of the difference in the flow parameters were calculated. Here, U is the magnitude of the local velocity ($U = \sqrt{u^2 + v^2}$). The standard deviation of the elevation, σ_z, was also calculated. The parameter σ_z indicates the magnitude of the elevation error (2σ = 0.15 m), but is not completely identical to the magnitude of the model elevation error since σ_z is impacted by the grid size and the spatial filtering effect due to gridding. The results are listed in Tables 2, 3, and 4 for the Plain, Rural, and Urban cases, respectively.

For a case of Plain topography (Table 2), the elevation of NoError cases has no undulation and is completely plain. Therefore, the standard deviation of the 05m-NoError and 10m-NoError cases indicates that the error due to discretization and the magnitude of the standard deviations are sufficiently small. The deviations in water depth and water level are comparable to one another and are increasingly proportional to the increment of the grid size. As shown in Figure 15, the water depth range spanned 0.0 to 0.3 m, and the standard deviations for water depth, σ_h, and water level, σ_H, were small relative to the water depth magnitude. With the exception of the area close to the inflow boundary, the flow rate per unit width, hU, was found to be in the range from 0.0 to 0.3 m^2/s. The relative magnitude of σ_{hU} in NoError cases was sufficiently small. The standard deviation of the momentum flux per unit width, σ_{hUU}, was one order larger than those of σ_{hU} for the 05m-NoError and 10m-NoError cases. The results shown in Table 2 imply that the flow parameters were quite sensitive to elevation uncertainty and that local flow parameters related to flow motion were almost unreliable under the presence of the elevation uncertainty.

The result of the Rural case, as indicated in Table 3, showed similar trends as for the Plain case. However, the σ_{hU} and σ_{hUU} for 05m-NoError in the Rural case were comparably larger than those for the 05m-NoError in the Plain case. Inundated water overflowed at the ribbing and was locally accelerated around the critical-section at the overflow point. The flow condition of the overflow was determined by the local topography surrounding the ribbing. Therefore, the small difference of the ribbing representation made a large difference on the overflow condition. Circulation in the rice field cell following overflow at the ribbing was quite sensitive to the overflow condition and led to a larger σ_{hU} and σ_{hUU}. Inundated water is stored in the rice field cell before overflow to the next paddy

435 begins, such that the range of water depth in rural cases reaches 0.5 m. The relative magnitude of the
436 standard deviation of the water depth is small. In this context, if the ground elevation distribution has
437 a distinct structure, such as rice field cells separated by ribbing in the Rural topography, the
438 inundated water will be stored in the areas surrounded by the ribbing (structured dents). The
439 location, area, and water storage capacity of the structured dents are almost conserved under the
440 influence of small elevation uncertainty. Therefore, the water level of the inundation water stored in
441 the structured dents is also not very sensitive to small grid errors. On the other hand, the unit width
442 discharge and momentum flux are sensitive to elevation uncertainty because the flow is accelerated
443 mainly at the boundary between consecutive structured dents (see Figure 20). The flow acceleration
444 is regulated by local ground elevation surrounding the ribbing. Thus, small elevation error at the
445 overflow points causes major changes in the direction and magnitude of local inundation flow.
446 The error magnitude of the calculated water depth, due to elevation error, can be estimated as
447 proportional to the magnitude of the elevation uncertainty. The error in water stage (σ_H) is
448 comparable to water depth uncertainty (σ_h), and, thus, the uncertainty in elevation (σ_z). Obviously,
449 there are close relationships among water stages, water depth, and elevation, namely, $H = z + h$.
450 Similar magnitudes for σ_h, σ_H, and σ_z imply that there are correlations amongst h', H', and z'.
451 To confirm the flow structure and its relationship to prediction error, the relationship between flow
452 parameters at t = 1000 s and a distance from the inflow point l are depicted in Figure 24. In Figure
453 24a, the water stage profile of the 03m-No error case is plotted. A systematic trend can be observed
454 in the profile of the water stage. Each cluster of the plot corresponds to the water stored in each
455 paddy cell. Figure 24b shows the distribution of the root mean square (RMS) of the water stage
456 errors, defined as follows:

457 $$H'_{\mathrm{RMS}} = \frac{1}{3}\sum_{j=A,B,C}\sqrt{\frac{1}{N_{(j)}}\sum_{i}^{N(j)}\left(H_{\mathrm{Err}(j)} - H_{\mathrm{NoErr}}\right)^2}\ . \qquad (6)$$

458 H'_{RMS} is the average error of the three elevation errors. The H'_{RMS} plot shows a weak relationship for
459 the systematic bias observed in Figure 24a, and the water stage error is kept at a constant level using
460 increments of distance from the inflow. The unit width discharge distribution is shown in Figure 24c.
461 In the area close to inflow (l < 200 m), a large unit width discharge shatter was observed and
462 corresponds to jet flow surrounding the inflow point. The plot of the RMS error of the unit width
463 discharge (Figure 24d) shows a similar profile and magnitude for the original unit width discharge
464 plot (Figure 24c). In the area far from inflow (l > 300 m), the RMS error of unit width discharge
465 keeps an almost constant level such as the error of the water stage. One should note that in the area
466 away from the flow inflow point (l > 300 m), the order of the original unit width discharge, hU, and
467 the magnitude of the error, hU'_{RMS}, are almost identical - indicating that local flow is quite uncertain
468 in cases where the elevation contains uncertainty.

The standard deviations of hU for Urban topography (as shown in Table 4) are small as compared to the Rural case. In the case of Urban topography, the arrangement of the buildings and road networks were kept almost constant among the different grid sizes and elevation error patterns. Inundation flow was regulated by the arrangement and the buildings, and the elevation distribution and horizontal topographical features had a smaller impact on the inundation. Therefore, there was a relatively smaller error for the unit width flow rate and momentum flux predictions for the Urban case. However, the magnitudes of the unit width flow rate and the momentum flux were around hU = 0.3 m^2/s and hUU = 0.3 m^3/s^2. Therefore, the standard deviations of hU and hUU in cases that contained elevation errors were relatively large ($\frac{\sigma_{hU}}{hU} \approx 0.2, \frac{\sigma_{hUU}}{hUU} \approx 0.4$). Standard deviations for water depth were comparable to elevation uncertainty in cases with elevation errors. A similar trend was observed for the Plain and Rural cases.

In order to investigate the spatial bias of the flow and the prediction uncertainty in the Urban case, the relationship between distance from the inflow and the flow parameters are depicted in Figure 25. The structure of the water stage profile shown in Figure 25a illustrates that a continuous but fluctuating downward trended water profile was observed along the street network. The water-stage error shown in Figure 25b shows a slight increasing trend with the increment of distance. In Figure 25c, the profile of the unit width discharge indicates that certain measurements of inundated water have a small unit width discharge, but that a larger unit width discharge is concentrated on the specific street. As depicted in the bright texture in Figure 23, the profile also indicates that most of the water mass is transferred to the specific flow network. The unit width discharge error shown in Figure 25d shows a similar pattern to the distribution shown in Figure 25c. The unit width discharge error at the propagating edge (l > 400 m) is raised and indicates that local flow at the propagating front has a comparatively large uncertainty.

Differences in topographical structure have a great impact on inundation flow propagation and the characteristics of prediction uncertainty, as shown in the differences in the profiles between Figure 24 and Figure 25, indicating that inundation flow has a structure and that inundation flow structure has a close relationship to topographical structure. A further important point is that the magnitude of the prediction uncertainty is also strongly regulated by topographical structure.

5. Conclusion

In this work, the effect of elevation uncertainty on predicted inundation flow was evaluated. Three representative topographies were designed. The sensitivities of grid size and elevation error to the calculated flow were investigated from the view point of the inundated area increment, the water depth distribution, the flow structure, and the quantitative evaluation of local flow parameters. The results suggest the following:

(1) The result calculated by the larger grid size displayed a shallower and faster water propagation of inundation as compared to the result calculated using a finer grid with the same roughness parameter, because rapidly-varied 2D flow is inadequately resolved using a coarse grid calculation. The smoothing effect of the elevation distribution also caused shallow and rapid inundation propagation in cases where a coarse grid size was utilized. Calibration of the roughness parameter is essential for adjusting the effect of grid size on the inundation propagation in cases where a large grid size is utilized.

(2) When the elevation distribution has a large scale structure (e.g. the structured dents in Rural topography, and the street network in Urban topography), inundation flow is regulated by the structure of the topography. The large-scale topographical structure is well kept within spatial features and is insensitive under the influence of elevation uncertainty. Therefore, water depth and water level can be predicted using a comparatively high accuracy in cases of inundation on structured topography, as compared with flow estimations in Plain topography. Since the acceleration of flow occurs in specific areas and since small differences in topography in specific areas cause a major change in inundation flow structure, local flow and flow related parameters suffer a great impact due to elevation error.

(3) The predicted local water depth, h, contains an uncertainty whose magnitude is almost identical to the magnitude of the elevation uncertainty. The standard deviation of hU is impacted both by elevation error and topographical structures. The magnitude of the standard deviation of hU is comparable to the magnitude of hU in cases where the topography has an elevation uncertainty. The σ_{hUU} is almost two-times larger than σ_{hU} in cases where the elevation has uncertainty. The relative error of the momentum flux is large as compared to that in the unit width discharge.

The work presented here implies that some part of the calculated flow parameters contain significant uncertainty. Therefore, the results obtained from this work should be kept in mind when flow parameters calculated using a detailed inundation simulation are used for risk estimations related to the flow velocity (e.g. the difficulty evacuation (Koshimura et al., 2006) or the risk failure for structures (Koshimura et al., 2009)). On the contrary, the reason inundated water was mainly utilized in the risk estimation may be related to the poor accuracy of the magnitude of predicted inundation flow. Research on inundation flow structure (Tsubaki et al., 2007) may be useful for determining key factors of topography that determine inundation expansion. By considering the dominant factor of topography, it may be possible to improve both the calculation efficiency and the accuracy, not only for detailed inundation flow type simulations but also for integrated type simulations in inundation prediction methods (e.g. Yu and Lane, 2005). The effect of topographical uncertainty in adverse sloped ground is not discussed in this paper but important area to be analysed to advance our knowledge of structural damage risk estimation in tsunami disaster.

Discussion in this work is limited to a comparison of the calculated results. A comparison with the field record or experimental data is not included mainly because the discussion presented in this work is quite sensitive to boundary condition uncertainty, and because it is quite difficult to determine sufficient accuracy and resolution for boundary conditions of actual inundation cases or physical models for complex topography inundation. The inadequacy of the calculation model itself is also outside the scope of this work. Here, the discussion has limitations for some of the conditions described above. However, the findings obtained in this study contribute to our understanding of the characteristics of the uncertainty involved in the predicted flow parameters under the effect of topographical data uncertainty. The predictability of local flow parameters on inundation flow within complex topography has not, thus far, been seriously addressed. The results obtained from this study indicate that more careful considerations should be made regarding the uncertainty of calculated results since calculated flow parameters, especially those related to water velocity, contain large uncertainty.

Elevation accuracy can be improved in regards to instrument improvement, operational control (e.g. lower and slower flight in aerial LiDAR measurements), and refined post-process of the measured data. Such improvements may, in some respects, reduce the error of the calculated result. On the other hand, physical uncertainty, for example, terrain alternation after the topography survey such as for vegetation growth or decay and for changes in the arrangements of parked cars and temporal structures, still remains after the improvement of accuracy in topography measurements. Again, we must acknowledge that calculated flow dynamics contain considerable uncertainty for cases where the predicted flow dynamics are utilized to predict risks related to water flow.

REFERENCES

Abdullah, A.F., Vojinovic, Z. and Price, R.K., 2011, Improved Methodology for Processing Raw LIDAR Data to Support Urban Flood Modelling - Accounting for Elevated Roads and Bridges, *Journal of Hydroinformatics*, doi:10.2166/hydro.2011.009.

Alcrude, F and Garcia-Navarro, P., 1993, A high-resolution Godunov-type scheme in finite volumes for the 2D shallow-water equations, *International Journal for Numerical Methods in Fluids*, 16, 489-505.

Anastasiou, K. and Chan, C.T., 1997, Solution of the 2D shallow water equations using the finite volume method on unstructured triangular meshes, *International Journal for Numerical Methods in Fluids*, 24, 1225-1245.

Bales, J.D. and Wagner, C.R. 2009, Sources of uncertainty in flood inundation maps, Journal of *Flood Risk Management*, 2, 139-147.

575 Bates, P.D., Horritt, M. and Hervouet, J.M., 1998, Investigating two-dimensional, finite element
576 predictions of floodplain inundation using fractal generated topography, *Hydrological Processes*,
577 12, 1257-1277.
578 Bates, P.D., 2003, Remote sensing and flood inundation modeling. *Hydrological Processes*, 18(13):
579 2593-2597.
580 Cabral, B. and Leedom, L., 1993: Imaging vector fields using line integral convolution, *Proc. 20th*
581 *annual conf. on Computer graphics and interactive techniques SIGGRAPH 93*.
582 Caleffi, V., Valiani, A. and Zanni, A., 2003, Finite volume method for simulating extreme flood
583 events in natural channels, *Journal of Hydraulic Research*, 41(2), 167-177.
584 Casas, A., Lane, S.N., Yu, D. and Benito, G., 2010, A method for parameterizing roughness and
585 topographic sub-grid scale effects in hydraulic modeling from LiDAR data, *Hydrology and Earth*
586 *System Science*, 14, 1567-1579.
587 Chuntian, C., Chunping, O. and Chau, K.W., 2002, Combining a fuzzy optimal model with a genetic
588 algorithm to solve multiobjective rainfall-runoff model calibration, *Journal of Hydrology*,
589 268(1-4), 72-86.
590 Cobby, D.M., Mason, D.C., Horritt, M.S. and Bates, P.D., 2003, Two-dimensional hydraulic flood
591 modelling using a finite-element mesh decomposed according to vegetation and topographic
592 features derived from airborne scanning laser altimetry, *Hydrological Processes*, 17, 1979-2000.
593 Fournier, A, Fussel, D, and Carpenter, L., 1982, Computer Rendering of Stochastic Models.
594 *Communications of the ACM*, 25: 371-384.
595 Horritt, M.S. and Bates, P.D., 2001, Effects of mesh resolution on a raster based model of flood
596 flow, *Journal of Hydrology*, 253, 239-249.
597 Horritt, M.S., Bates, P.D. and Mattinson, M.J., 2006, Effects of mesh resolution and topographic
598 representation in 2D finite volume models of shallow water fluvial flow, *Journal of Hydrology*,
599 329, 206-314.
600 Horritt, M.S., 2006, A methodology for the validation of uncertain flood inundation models, *Journal*
601 *of Hydrology*, 326, 153-165.
602 Koivumäki, L., Alho, P., Lotsari, E., Käyhkö, J., Saari, A. and Hyyppä, H., 2010, Uncertainties in
603 flood risk mapping: a case study on estimating building damages for a river flood in Finland,
604 *Journal of Flood Risk Management*, 3, 166-183.
605 Koshimura, S., Katada, T., Mofjeld, H.O. and Kawata, Y. 2006, A method for estimating casualities
606 due to the tsunami inundation flow, *Natural Hazards*, 39, 265-274.
607 Koshimura, S., Oie, T., Yanagisawa, H. and Imamura, F., 2009, Developing fragility functions for
608 tsunami damage estimation using numerical model and post-tsunami data from Banda Aceh,
609 Indonesia, *Coastal Engineering Journal*, 51(3), 243-273.

610 Mason, D.C., Horritt, M.S., Hunter, N.M. and Bates, P.D., 2007, Use of fused airborne scanning
611 laser altimetry and digital map data for urban flood modeling, *Hydrological Processes*, 21,
612 1436-1447.
613 McKean, J., Nagel, D., Tonina, D., Bailey, P., Wright, C.W., Bohn, C. and Nayegandhi, A. 2009,
614 Remote se sing of channels and riparian zones with a narrow-beam aquatic-terrestrial LiDAR,
615 Remote Sensing, 1, 1065-1096, doi:10.3390/rs1041065.
616 Mignot, E., Paquier, A. and Haider, S., 2006, Modeling floods in a dense urban area using 2D
617 shallow water equations, *Journal of Hydrology*, 327, 186-199.
618 Neal. J.C., Bates, P.B., Fewtrell, T.J., Hunter, N.M., Wilson, M.D. and Horritt, M.S., 2009,
619 Distributed whole city water level measurements from Carlisle 2005 urban flood event and
620 comparison with hydraulic model simulations, *Journal of Hydrology*, 368, 42-55.
621 Neal, J.C, Fewtrell, T.J, Bates, P.B. and Wright, N.G. 2010, A comparison of three parallelization
622 methods for 2D flood inundation models, *Environmental Modelling & Software*, 25: 398-411.
623 Néelz, S., Pender, G., Villanueva, I., Wilson, M., Wright, N.G., Bates, P., Mason, D. and Whitlow,
624 C., 2006, Using remotely sensed data to support flood modelling, *Water Management*, 159, Paper
625 14106.
626 Pasternack, G.B., Gilbert, A.T., Wheaton, J.M. and Buckland, E.M. 2006, Error propagation for
627 velocity and shear stress prediction using 2D models for environmental management, *Journal of*
628 *Hydrology*, 328, 227-241.
629 Pappenberger, F., Beven, K.J., Horritt. M. and Blazkova, S. 2005, Uncertainty in the calibration of
630 effective roughness parameters in HEC-RAS using inundation and downstream level
631 observations, *Journal of Hydrology*, 302, 46-69.
632 Pappenberger, F., Beven, K.J., Ratto, M. and Matgen, P. 2009, Multi-method global sensitivity
633 analysis of flood inundation models, *Advances in Water Resources*, 31, 1-14.
634 Sanders, B.F, 2007, Evaluation of on-line DEMs for flood inundation modeling, *Advances in Water*
635 *Resources*, 30, 1831-1843.
636 Sanders, B.F., Schubert, J.E. and Detwiler, R.L. 2010, ParBreZo: A parallel, unstructured grid,
637 Godunov-type, shallow-water code for high-resolution flood inundation modeling at the regional
638 scale, *Advances in Water Resources*, 33, 1456-1467.
639 Schubert, J., Sanders, B.F., Smith, M.J and Wright, N.G., 2008, Unstructured mesh generation and
640 landcover-based resistance for hydrodynamic modeling of urban flooding, *Advances in Water*
641 *Resources*, 31, 1603-1621.
642 Schubert, J. and Sanders, B.F., 2012, Building treatments for urban flood inundation models and
643 implications for predictive skill and modeling efficiency, *Advances in Water Resources*, 41,
644 49-64.

645 Schumann, G., Matgen, P., Hoffmann, L., Hostache, R., Pappenberger, F. and Pfister, L. 2007,
646 Deriving distributed roughness values from satellite radar data for flood inundation modelling,
647 *Journal of Hydrology*, 344, 96-111.
648 Schumann, G., Cutler, M., Black, A., Matgen, P., Pfister, L., Hoffmann, L. and Pappenberger, F.,
649 2008, Evaluating uncertain flood inundation predictions with uncertain remotely sensed water
650 stages, *International Journal of River Basin Management*, 6(3), 187-199.
651 Shamseldin, A.Y., 1997, Application of a neural network technique to rainfall-runoff modeling,
652 *Journal of Hydrology*, 199(3-4), 272-294.
653 Shigeda, M, Akiyama, J, Ura, M, Jha, AK, and Arita, Y., 2002, Numerical simulations of flood
654 propagation in a flood plain with structures, *Journal of Hydroscience and Hydraulic Engineering*
655 20(2): 117–129.
656 Shige-eda, M. and Akiyama, J. 2003, Numerical and experimental study on 2D flood flows with and
657 without structures, *Journal of Hydraulic Engineering*, 129(10), 817–821.
658 Sithole, G. and Vosselman, G. 2004, Experimental comparison of filter alhorithms for bare-Earth
659 extraction from airborne laser scanning point clouds, *ISPRS Journal of Photogrammetry &*
660 *Remote Sensing*, 59, 85-101.
661 Soares-Frazão, S, Lhomme, J., Guinot, V. and Zech, Y. 2008, Two-dimensional shallow-water
662 model with porosity for urban flood modelling, *Journal of Hydraulic Research*, 46(1), 45-64.
663 Stephens, E.M., Bates, P.D., Freer, J.E. and Mason, D.C., 2012, The impact of uncertainty in
664 satellite data on the assessment of flood inundation models, Journal of Hydrology, 414-415,
665 162-173
666 Tsubaki, R, Fujita, I, and Okabe, T. 2007, Sensitivity of grid spacing to prediction and coherent flow
667 structure of inundation on urbanized area, *32rd Congress of IAHR*, on CD-ROM, Venice, 2007.
668 Tsubaki, R., Nakayama, Y. and Fujita, I., 2008, The design secret of kyokusui-no-en's meandering
669 channel, Journal of Visualization, 11(3), 265-272.
670 Tsubaki, R, and Fujita, I. 2010. Unstructured grid generation using LiDAR data for urban flood
671 modelling, *Hydrological Processes*, 24(11): 1404-1420.
672 Wagner, T., McIntyre, N., Lees, M.J., Wheater, H.S. and Gupta, H.V., 2003, Towards reduced
673 uncertainty in conceptual rainfall-runoff modelling: dynamic identifiably analysis, Hydrological
674 Processes, 17(2), 455-476.
675 Wu, C.L., Chau, K.W. and Li, Y.S., 2009, Methods to improve neural network performance in daily
676 flows prediction, *Journal of Hydrology*, 372(1-4), 80-93.
677 Yu, D. and Lane, S.N., 2005, Urban fluvial flood modelling using a two-dimensional diffusion-wave
678 treatment, part 1: mesh resolution effects, Hydrological Processes, 20(7) 1541-1565,
679 doi:10.1002/hyp.5935.
680

Figure captions

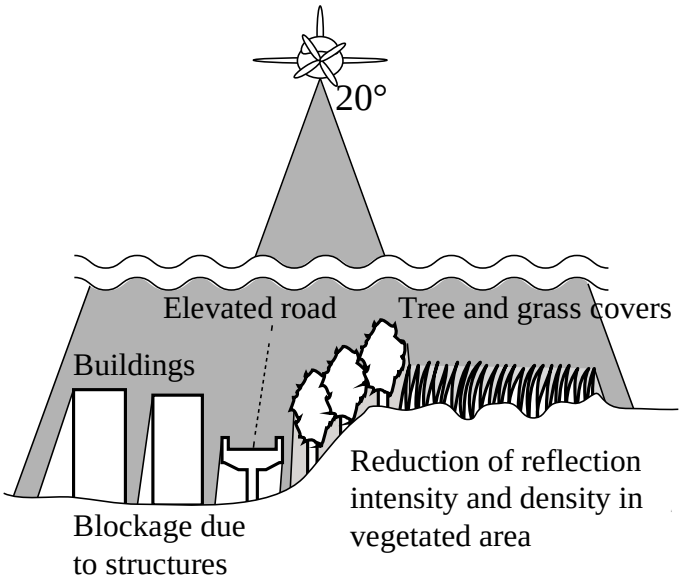

Figure 1**. Schematic diagram of lase pulse interference in LiDAR survey to detect ground surface.**

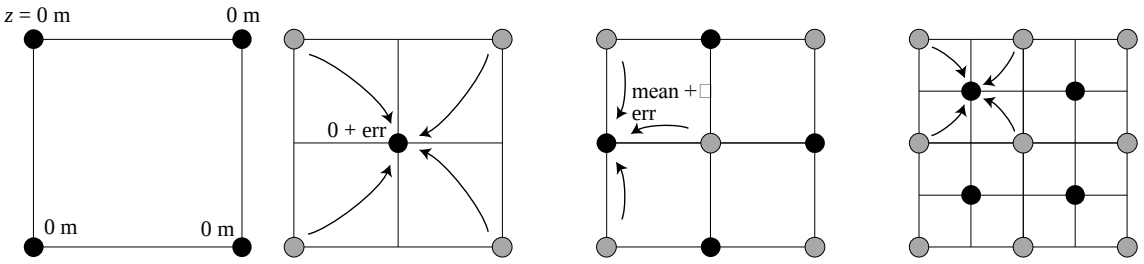

(a) The initial state

(b) The elevation at the center of the square was calculated using the mean of the elevations at the four corners of the square with the addition of the random component.

(c) The elevation at the center of a diamond was calculated using the mean of the elevations at the four corners of the diamonds with the addition of the random component.

(d) The square to diamond calculation

Figure 2**. The diamond-square algorithm for fractal topography generation.**

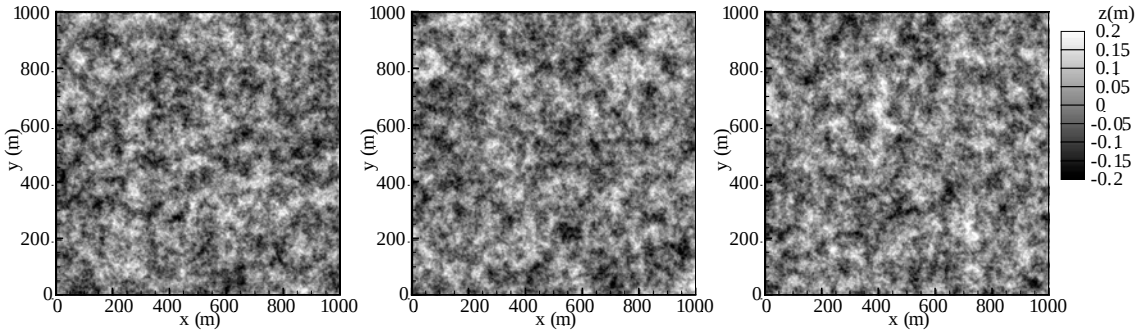

690 (a) ErrorA (b) ErrorB (c) ErrorC

691 **Figure** 3**. The generated fractal topography representing LiDAR measurement error. The**
692 **magnitude of the elevation fluctuation was set as σ = 0.075 m.**

693

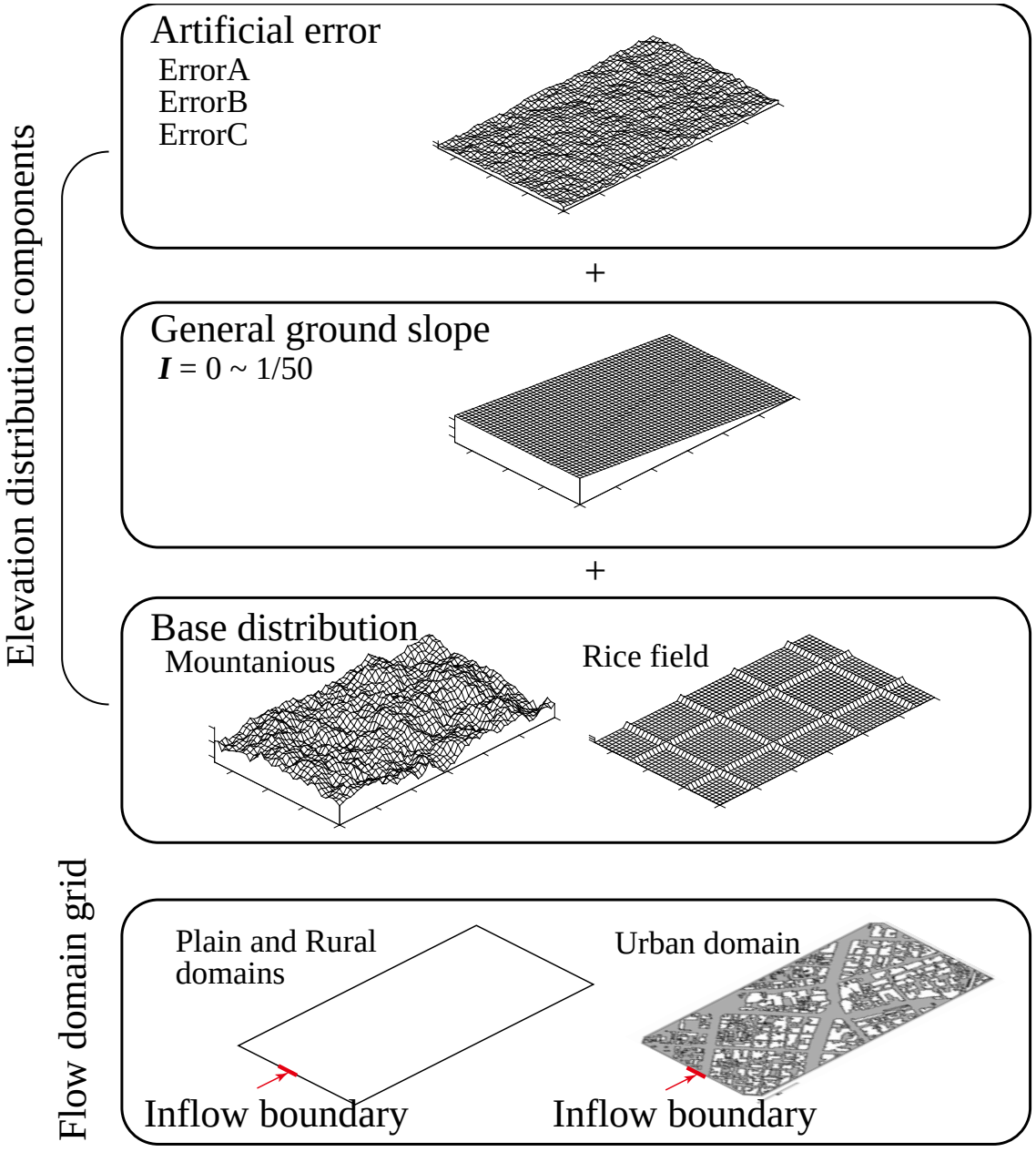

694

695 **Figure** 4**. A schematic of the topographical data set generation. Topographical data consists of**
696 **a gridded flow domain and an elevation distribution. For urban topography, an arrangement**
697 **of buildings is represented in the grid. The elevation distribution, consisting of the base**
698 **distribution, differs with each topographical case, the general ground slope, and the artificial**
699 **elevation error.**

700

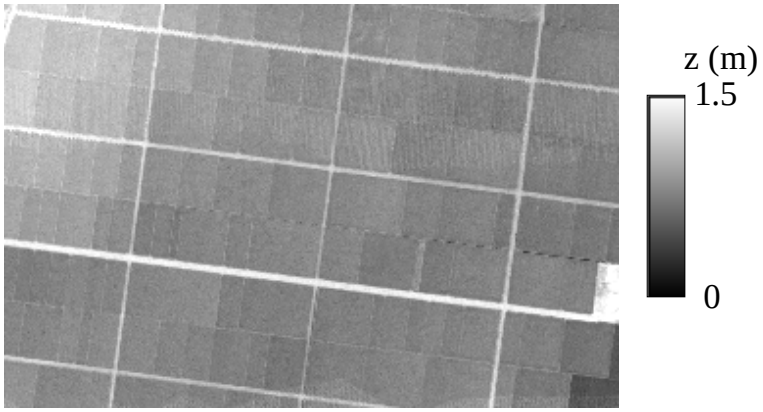

Figure 5**. The base distribution used for the rural topography. The elevation distribution was obtained from an actual LiDAR survey while measuring a rice field in Niigata, Japan.**

Figure 6**. The flow domain boundary utilized for urban topography. The topography was obtained from an actual LiDAR survey of the city of Hyogo, Japan. In this work, a building area was treated as an impermeable wall during inundation simulations.**

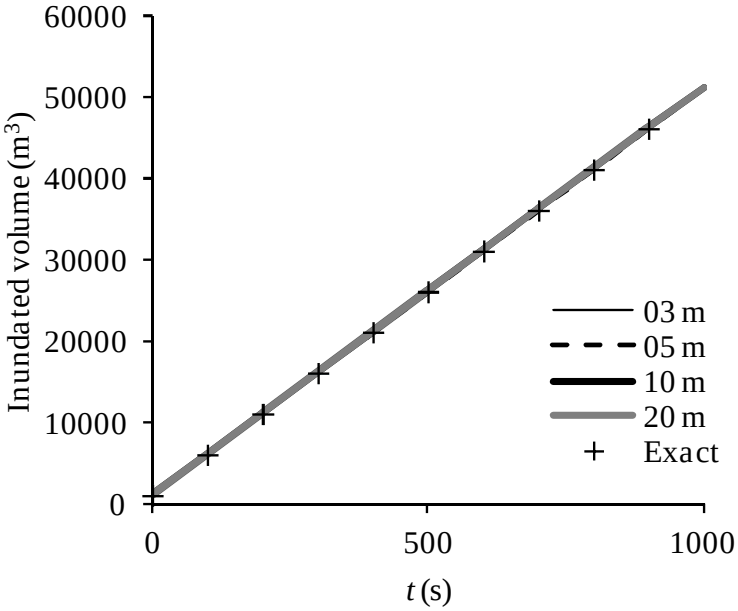

710

711 **Figure** 7**. The time-series of water volume in the calculation domain for the Plain case with *I* =**
712 **1/2000. The calculated results of the four grid sizes and the exact value are compared.**

713

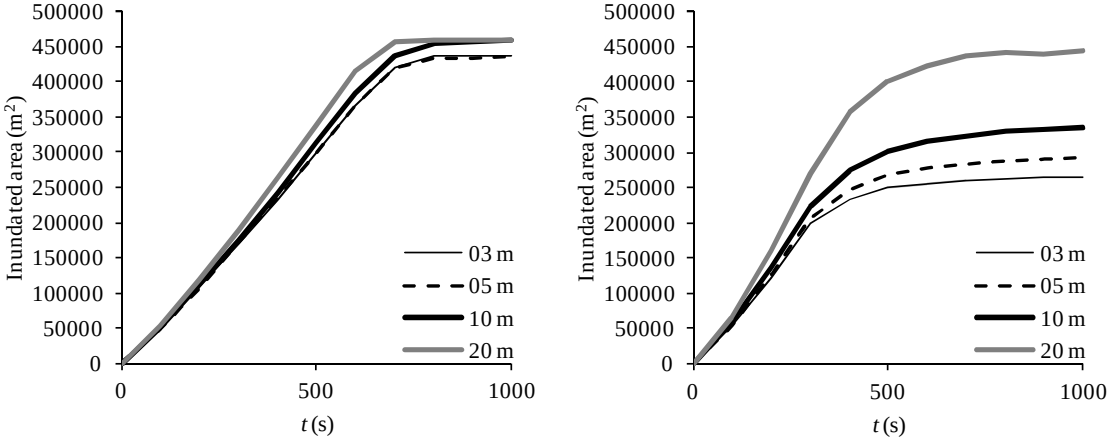

714 (a) I=1/300 (b) I=1/50

715 **Figure** 8**. Hydrographs of the inundated area. The left figure and the right figure compare the**
716 **results of the four grid sizes in a medium bed slope (*I* = 1/300) and a steep bed slope (*I* = 1/50),**
717 **respectively.**

718

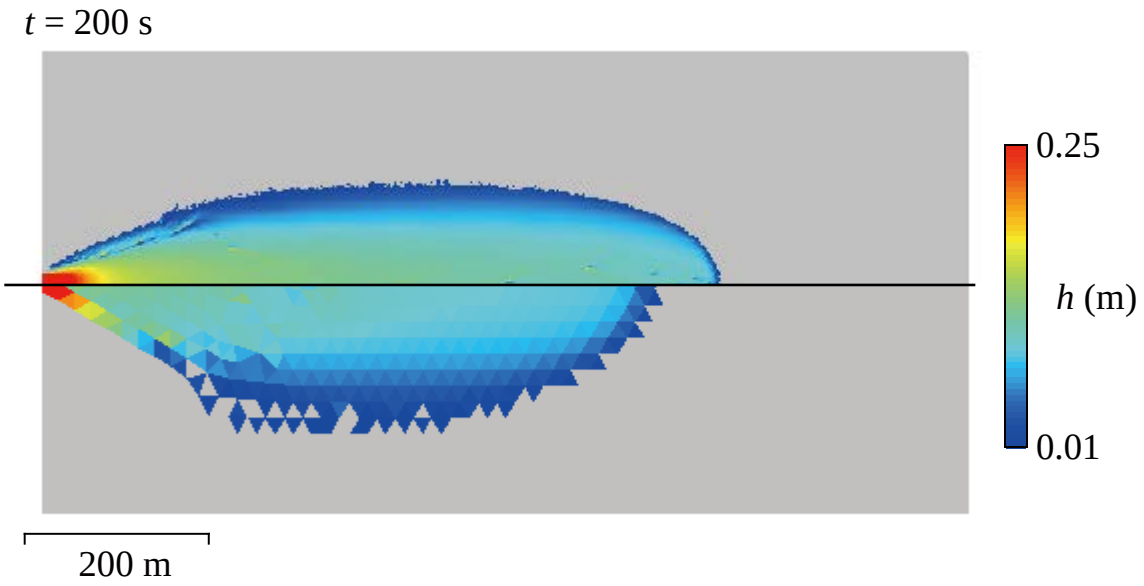

Figure 9**. A snap shot of the inundated water depth, *h*, at *t* = 200 s for a steep bed slope (*I* = 1/50) case. The upper half represents a small grid (the grid size is 3 m) result and the lower half provides a coarse grid (the 20 m in the grid size) result. The hatched areas indicate a dry region.**

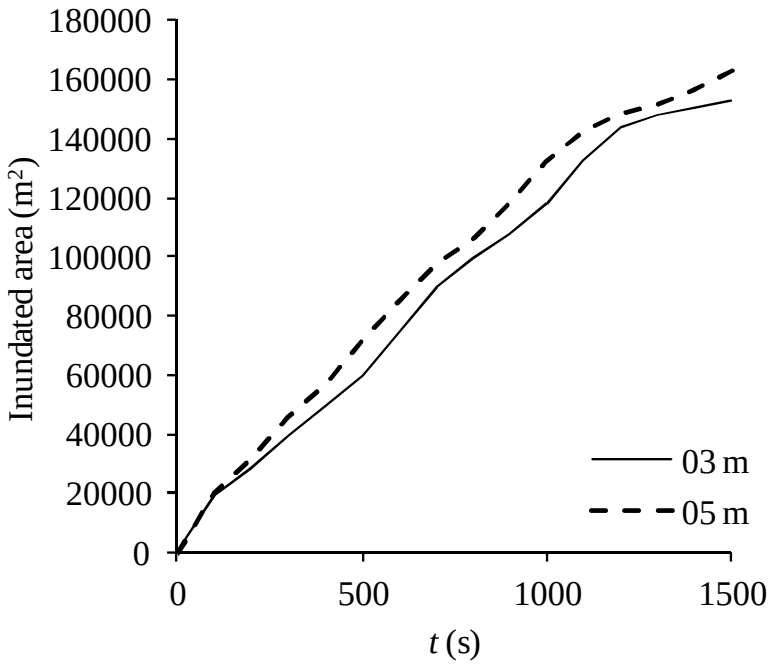

Figure 10**. The time series of the inundated area calculated using the two grid sizes.**

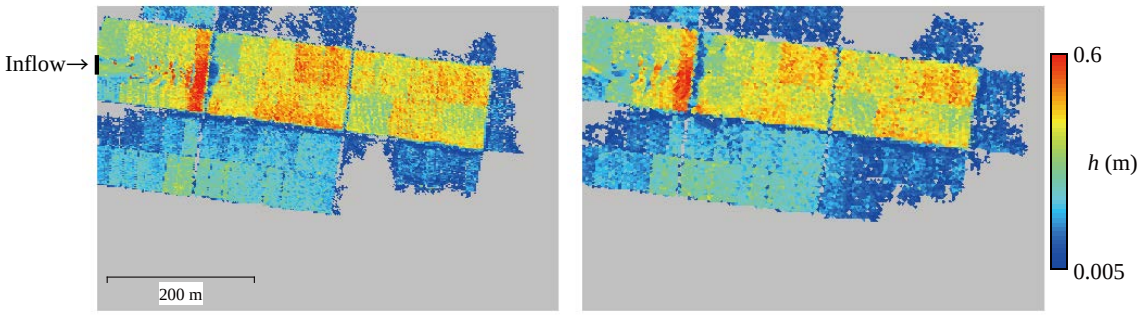

(a) 03 m grid (b) 05 m grid

728

729 **Figure** 11**. A snap shot of water depth at *t* = 1000 s, calculated using two grid sizes.**

730

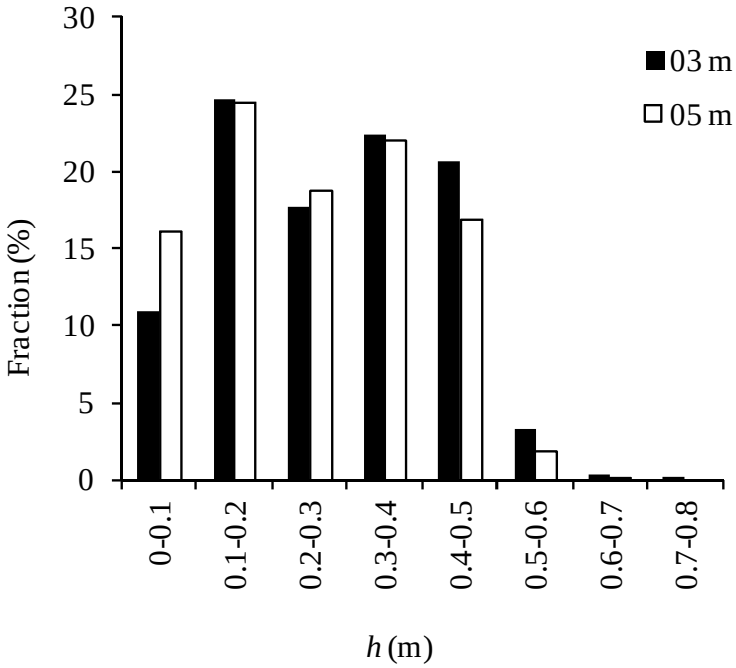

731

732 **Figure** 12**. A percentile distribution of the water depth distribution at *t* = 1000 s.**

733

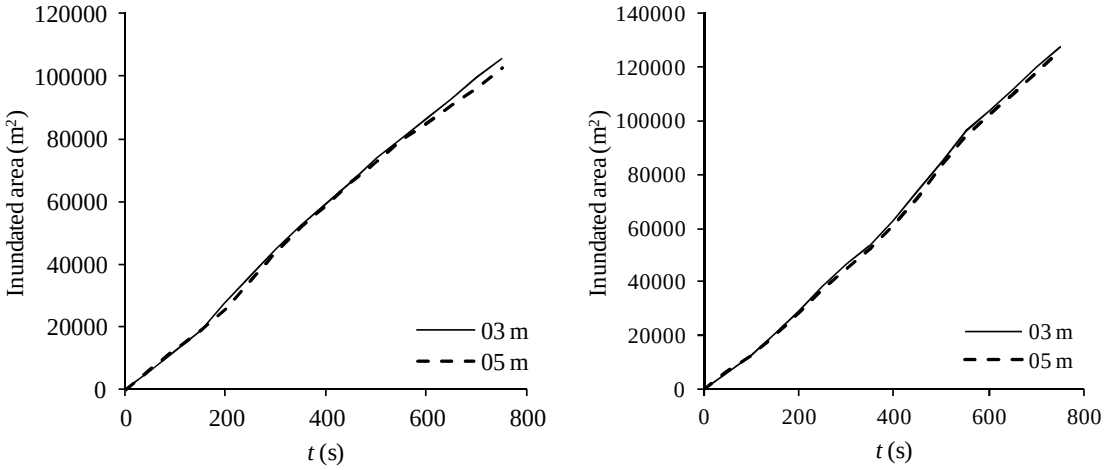

(a) I=1/50 (b) I=1/1000

Figure 13**. A time series of the inundated area for steep (left side sub-figure) and mild sloped (right side sub-figure) urban topographies, calculated using two grid sizes.**

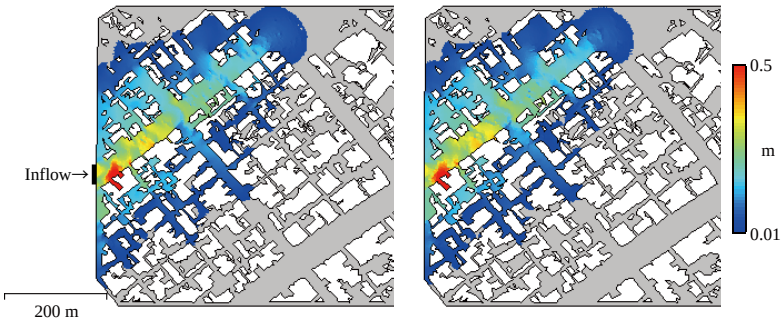

(a) 03 m grid (b) 05 m grid

Figure 14**. A snap shot of the inundated water depth at t = 400 s, for the mild bed slope (I = 1/1000) case.**

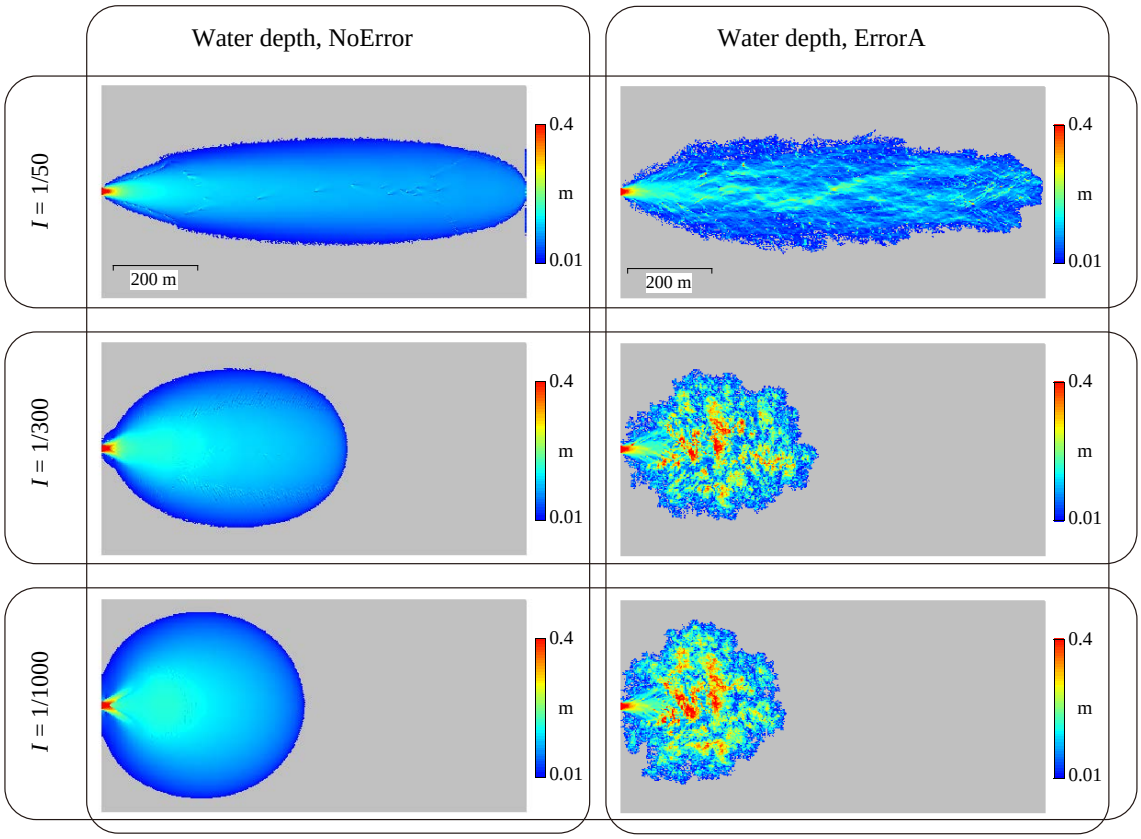

Figure 15**. A comparison of the general bed slope effect and the elevation noise; the left-hand side indicates no-additional-noise result; the right-hand side provides an additional noise A pattern. A snap shot is depicted at *t* = 300 s.**

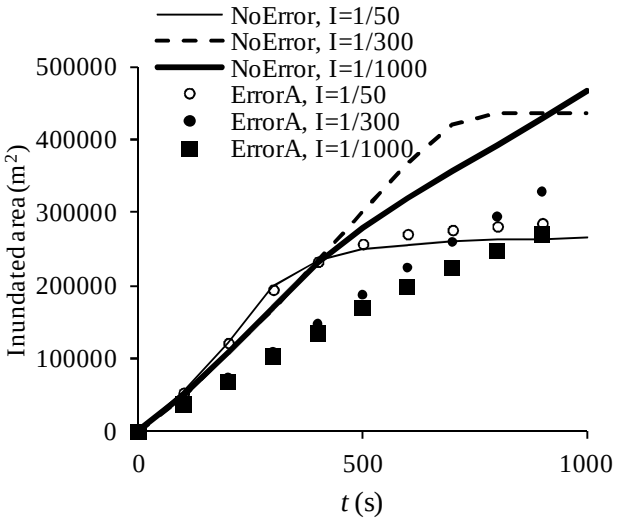

Figure 16. The time series of the inundated area for Plain topographies with and without elevation error and for different ground slopes.

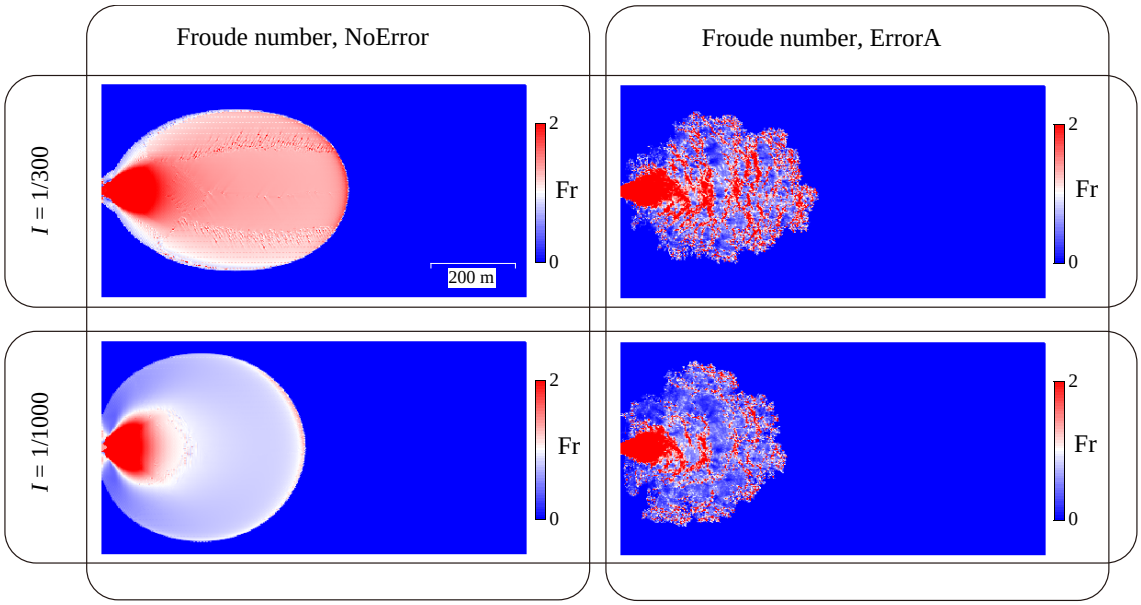

Figure 17**. A comparison of the Froude number distributions of the results calculated with and without elevation error. A snap shot at *t* = 300 s is shown.**

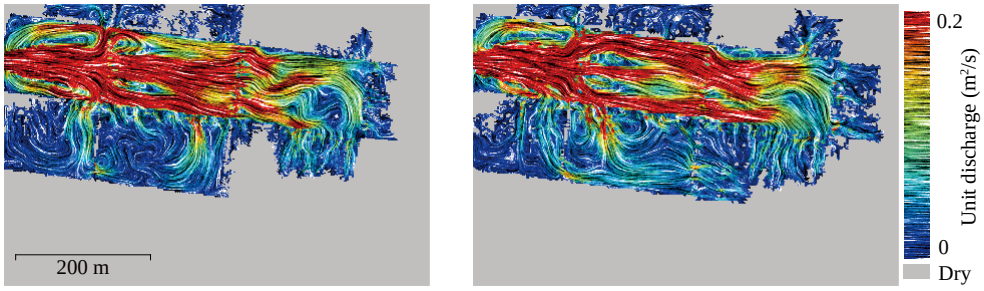

(a) 03m grid, NoError (b) 05m grid, NoError

(c) 03m grid, ErrorA (d) 03m grid, ErrorB

Figure 18**. A comparison of the flow structure at *t* = 1000 s, calculated using different grid sizes and different error patterns. Images were generated using the LIC (Line Integral Convolution) method. The direction of texture indicates the local flow direction. The density of the texture corresponds to the local discharge per unit width.**

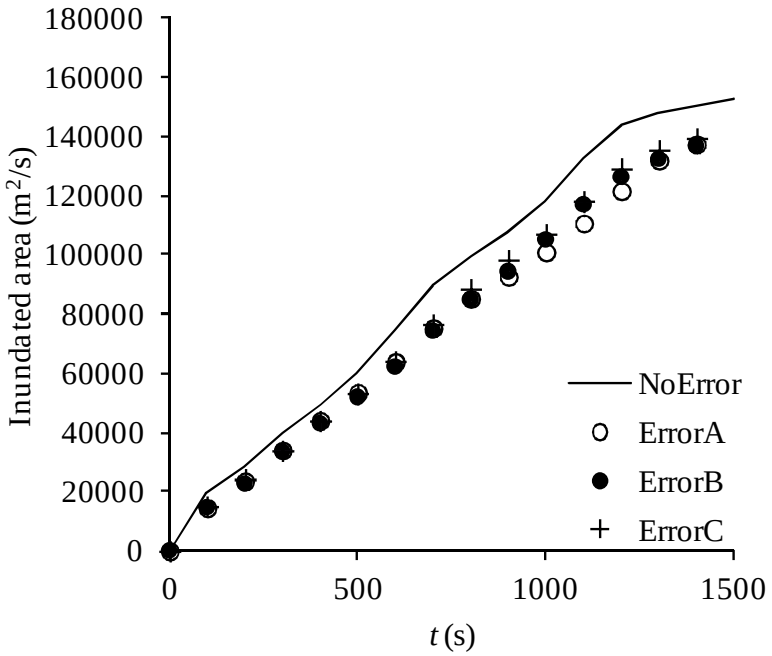

Figure 19**. A time series of the inundated area for Rural topographies with and without elevation error. The grid size is 03 m.**

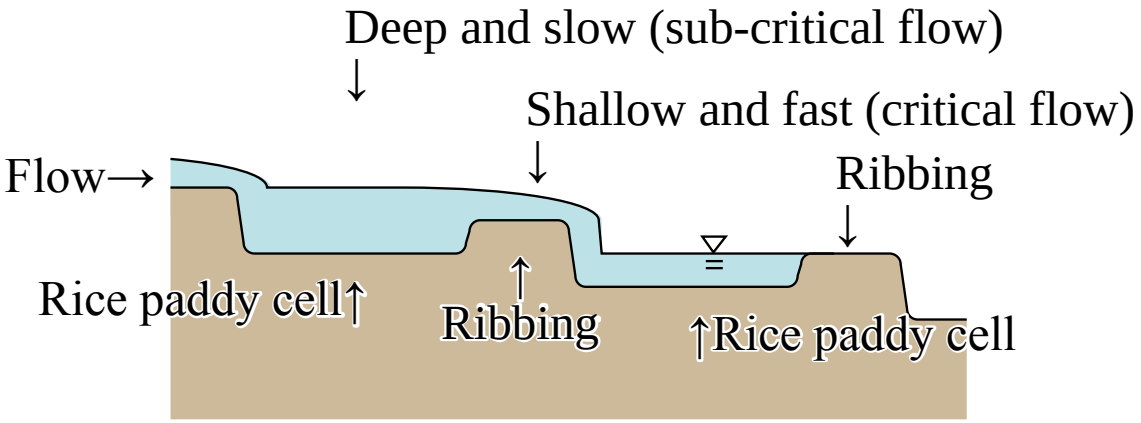

Figure 20**. A schematic diagram, vertical section, of the structure of inundation flow and its relationship to topography in Rural areas.**

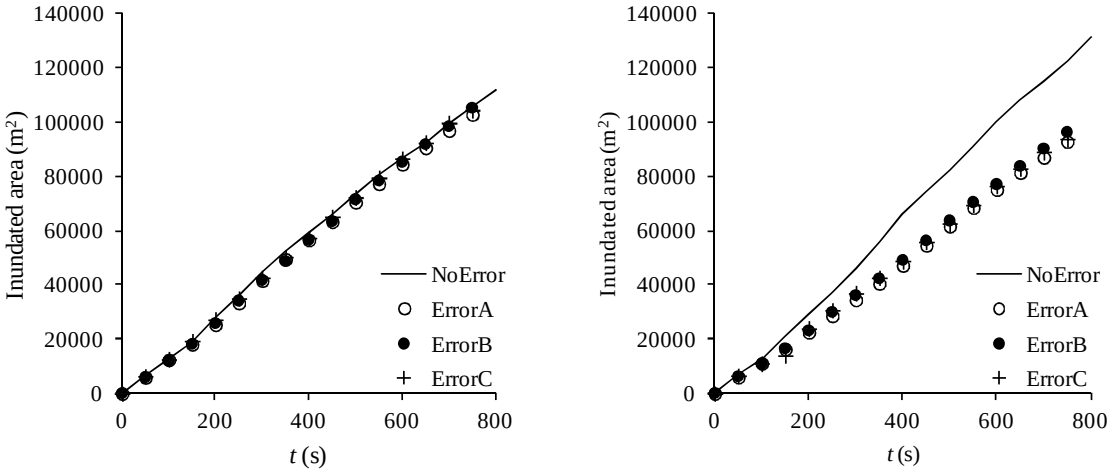

769

770 **Figure** 21**. A time series of the inundated area of Urban topographies for a steep slope (I =**
771 **1/50) and a medium slope (I = 1/300) with and without elevation error. The grid size is 03 m.**

772

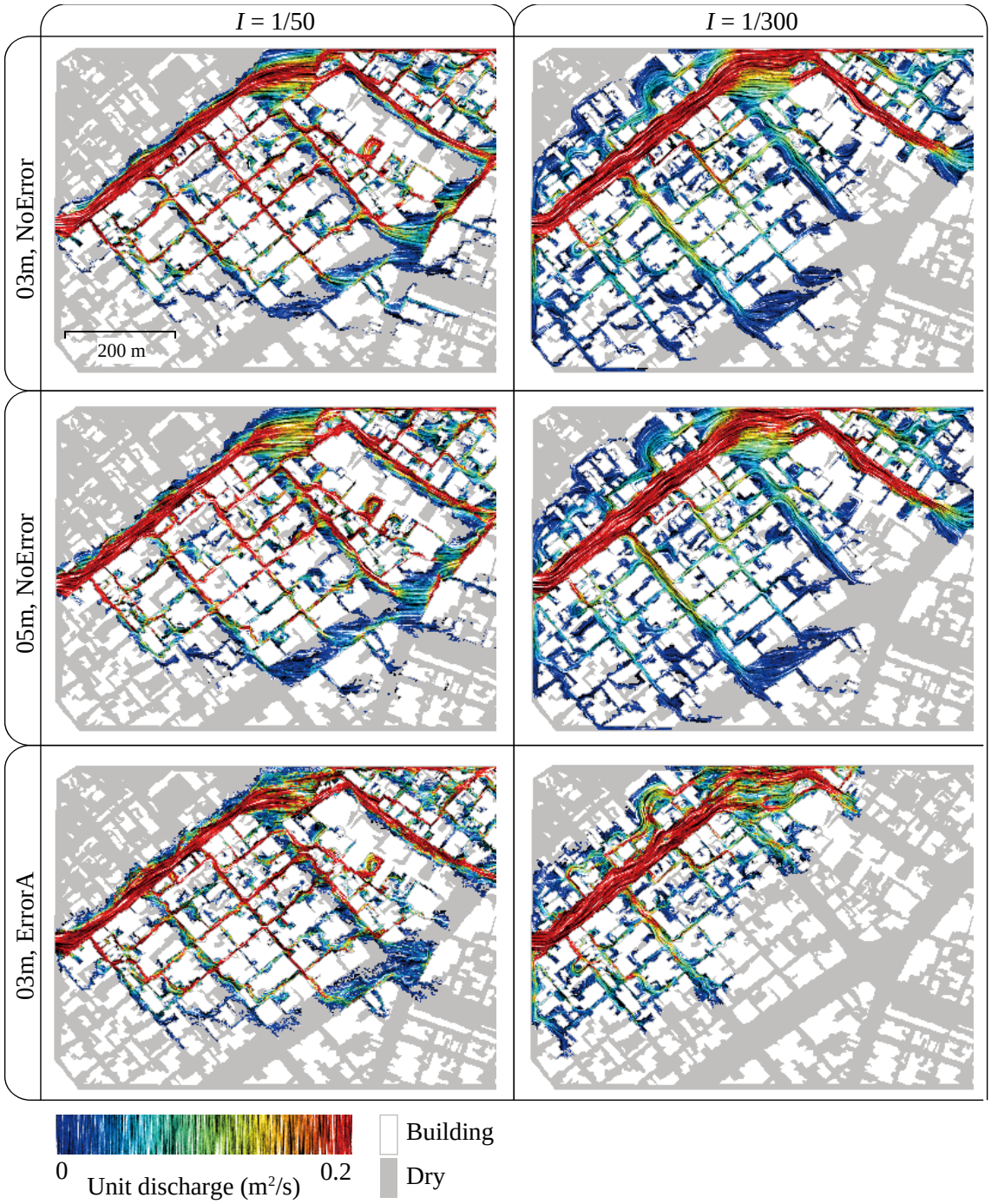

Figure 22. LIC images of urban topography cases calculated using different conditions at *t* = 800 s. The upper row provides the results calculated using a 03 m grid size without elevation error. The medium row provides results obtained using a 05 m grid without error. The lower row depicts results with a 03 m grid that contained elevation error. The left column provides the results of a steep slope (*I* = 1/50), and the right column provides the results of a medium slope (*I* = 1/300).

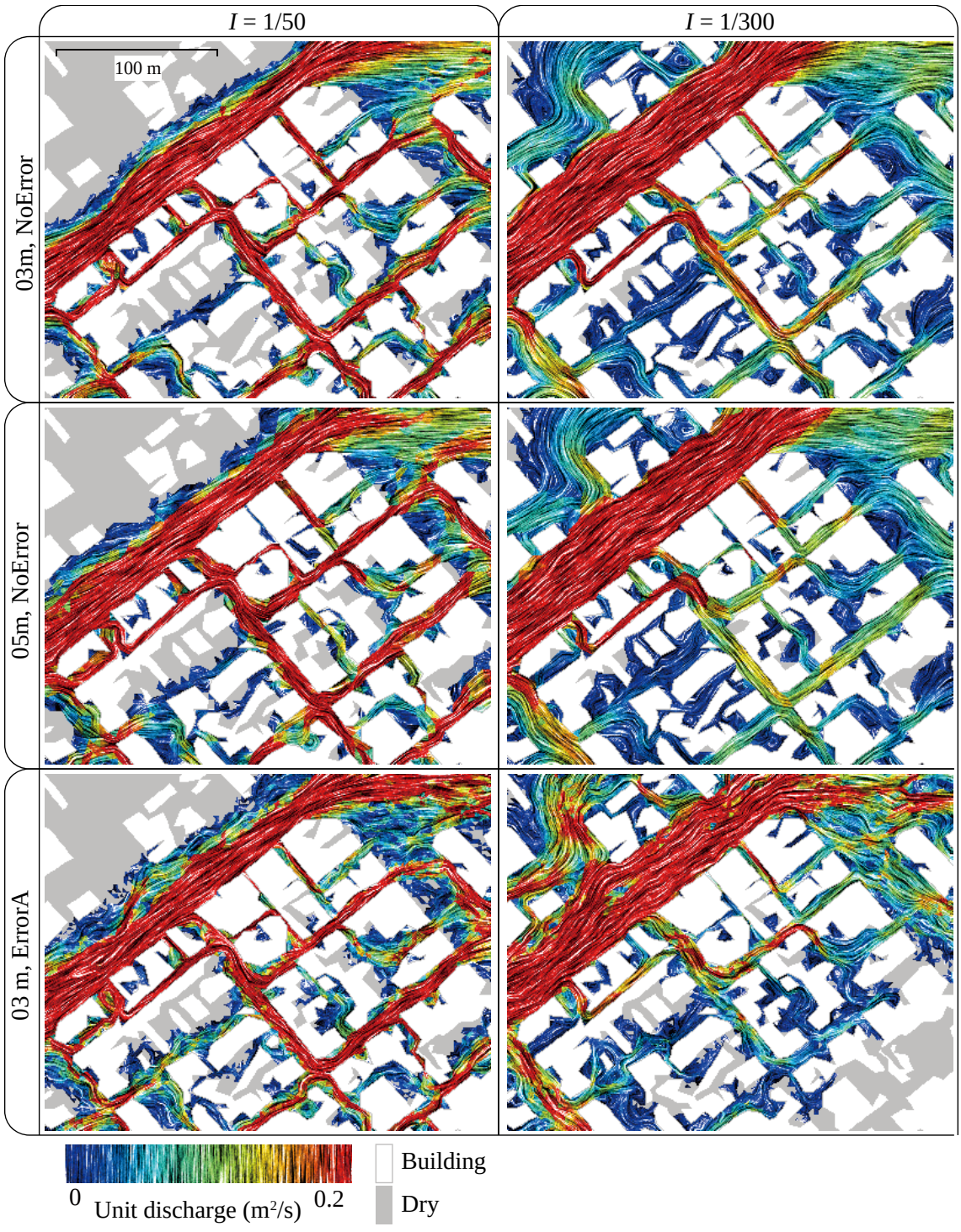

Figure 23. A close up of the inflow area of LIC images. The calculated conditions and the arrangement of the sub-figures are identical to those provided in Figure 21.

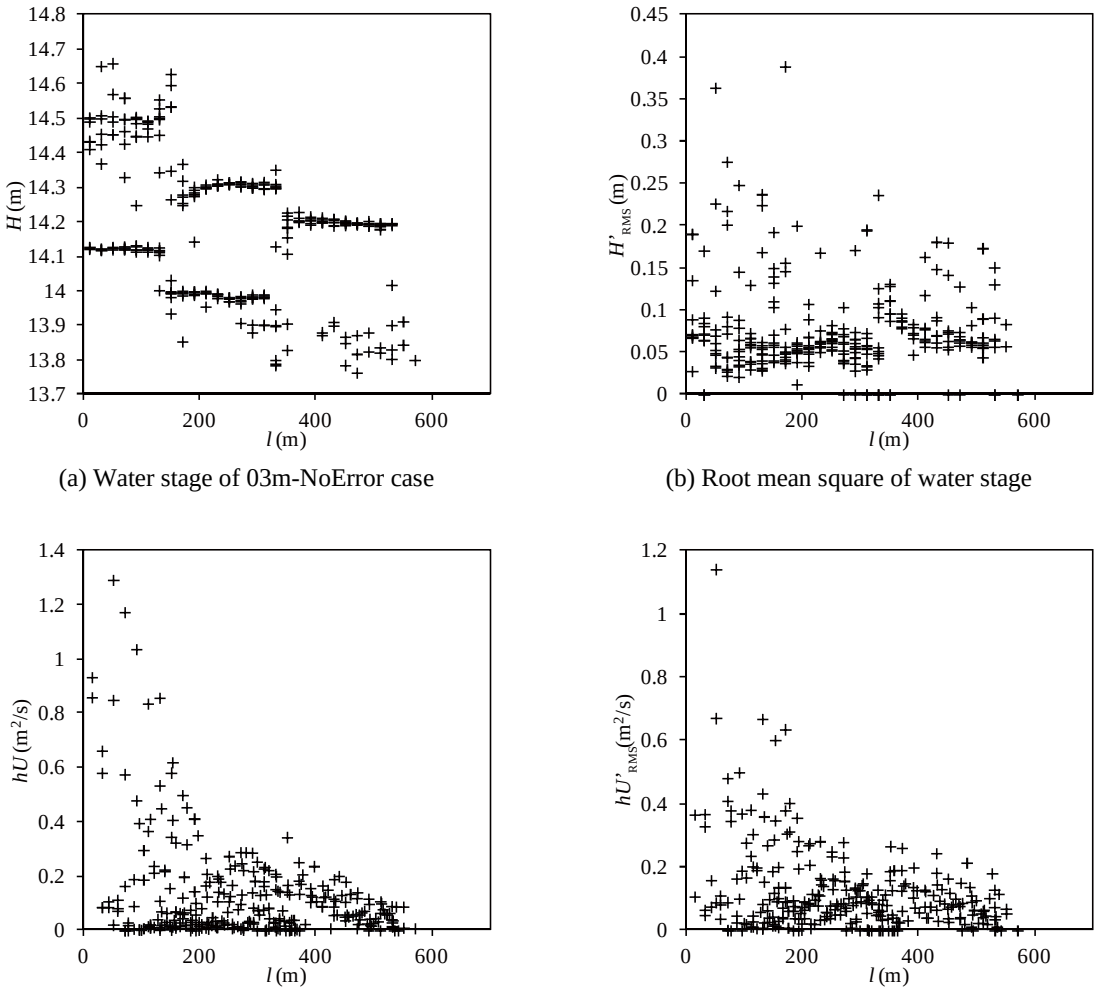

(a) Water stage of 03m-NoError case

(b) Root mean square of water stage

(c) Unit discharge of 03m-NoError case

(d) Root mean square of unit discharge

Figure 24**. The relationship between distance from the inflow point and the flow parameters, and errors at *t* = 1000 s for the Rural case. Sub-figures (a) and (c) display the distributions of the water stage and the unit width discharge of the base calculation (03 m-NoError). Sub-figures (b) and (d) depict the water stage and the unit width discharge errors calculated using the standard deviation error for the three elevation noise cases.**

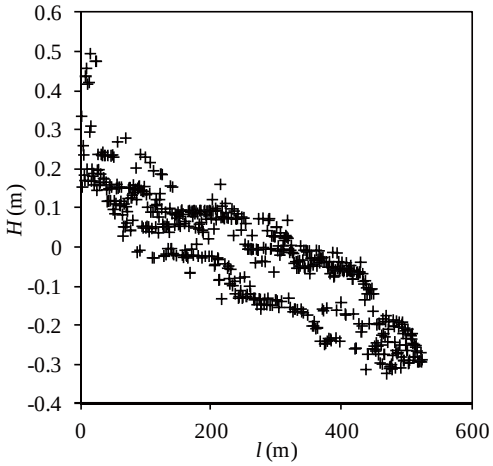

(a) Water stage of 03m-NoError case

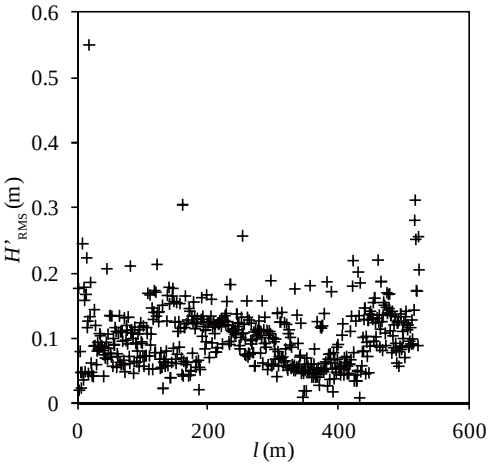

(b) Root mean square of water stage errors

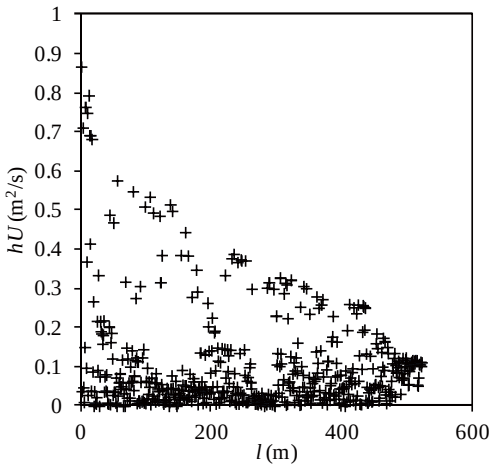

(c) Unit discharge of 03m-NoError case

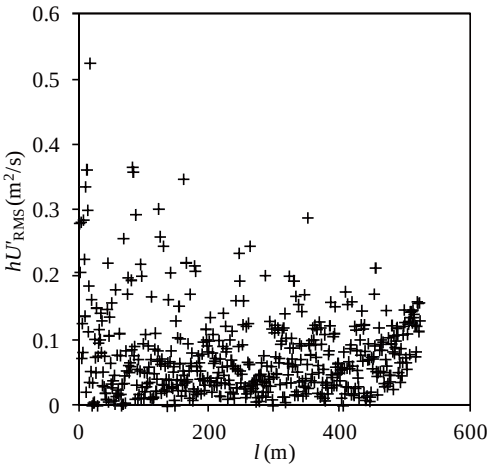

(d) Root mean square of unit discharge errors

Figure 25**. The relationship between distance from the inflow point and flow parameters, and those errors at *t* = 800 s for the Urban case of *I* = 1/1000. Sub-figures (a) and (b) provide the distributions of the water stage and the discharge par unit width of the base calculation (03m-NoError). Sub-figures (c) and (d) depict the water stage and the unit discharge errors calculated using the standard deviation error for the three elevation noise cases.**

Table captions

Table 1. The calculation case list

Topographical type	Additional slope *I*	Error pattern			
		No	A	B	C
Plain	1/2000	**3, 5, 10, 20**	**3**		
	1/1000	**3, 5, 10, 20**	**3**		
	1/300	**3, 5, 10, 20**	**3, 5, 10, 20**	**3**	**3**
	1/50	**3, 5, 10, 20**	**3, 5, 10, 20**		
Rural	0	**3, 5**	**3, 5**	**3, 5**	**3, 5**
	1/1000	**3, 5**			**3, 5**
	1/300	**3, 5**			**3, 5**
	1/50	**3, 5**			**3, 5**
Urban	1/1000	**3, 5**	**3, 5**	**3, 5**	**3, 5**
	1/300	**3, 5**	**3, 5**	**3, 5**	**3, 5**
	1/50	**3, 5**	**3, 5**	**3, 5**	**3, 5**

Number in thick box indicates the grid size of calculated case

Table 2. The standard deviations between local flow parameters at *t* = 300 s for the Plain case, *I* = 1/300. The result of the 03 m, NoError case is assumed to be a benchmark; and the difference between the 03m, No error case, and each case is indicated as a standard deviation.

		σ_z (m)	σ_h (m)	σ_H (m)	σ_{hU} (m^2/s)	σ_{hUU} (m^3/s^2)
05m	NoError	0.0012	0.0054	0.0081	0.018	0.133
10m	NoError	0.0022	0.0134	0.0124	0.041	0.356
03m	ErrorA	0.0648	0.0619	0.0736	0.101	0.403
03m	ErrorB	0.0595	0.0589	0.0796	0.081	0.322
03m	ErrorC	0.0628	0.0607	0.0813	0.104	0.418

n ≧ 282

Table 3. The standard deviations between local flow parameters at t = 1000 s for the Rural case. The data was processed using the method in Table 2.

		σ_z (m)	σ_h (m)	σ_H (m)	σ_{hU} (m^2/s)	σ_{hUU} (m^3/s^2)
05m	NoError	0.0333	0.0429	0.0589	0.112	0.241
03m	ErrorA	0.0659	0.0735	0.0552	0.104	0.190
03m	ErrorB	0.0638	0.0696	0.0538	0.087	0.159
03m	ErrorC	0.0675	0.0674	0.0543	0.114	0.272

n ≧ 283

822 **Table 4. Standard deviations between local flow parameters at *t* = 500 s for the Urban case, *I* =**
823 **1/1000. The data was processed using methods from Table 2.**
824

		σ_z (m)	σ_h (m)	σ_H (m)	σ_{hU} (m^2/s)	σ_{hUU} (m^3/s^2)
05m	NoError	0.0013	0.0141	0.0407	0.029	0.027
03m	ErrorA	0.0678	0.0661	0.0663	0.056	0.103
03m	ErrorB	0.0665	0.0636	0.0702	0.070	0.146
03m	ErrorC	0.0641	0.0636	0.0741	0.051	0.131

n ≧ 228

825
826